

# A 2.6 m Aqueous Electrolyte for High-Energy-Density Lithium-Ion Pouch Cells Using NbO<sub>2</sub> Anode

Published as part of ACS Energy Letters *special issue* "The Evolving Landscape of Energy Research: Insights from Leading Researchers".

Chuangyu Hou, Changming Ke, Runze Chen, Yangfan Lin, Qin Huang, Shi Liu,\* and Jianhui Wang\*



Cite This: <https://doi.org/10.1021/acsenerylett.5c03327>



Read Online

ACCESS |



Metrics & More

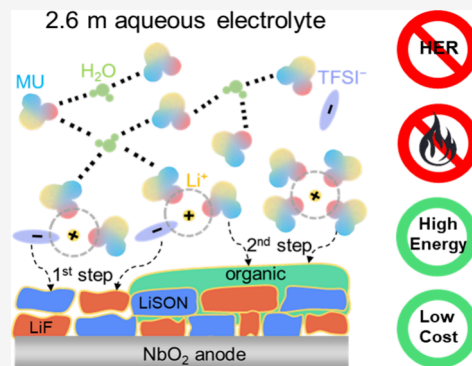


Article Recommendations



Supporting Information

**ABSTRACT:** Niobium-based oxides are promising high-energy-density anodes (>300 mAh g<sup>-1</sup> at 1.0–2.0 V vs Li<sup>+</sup>/Li) but face challenges with conventional aqueous electrolytes. Herein, we develop a cost-effective, dilute aqueous electrolyte modulated by methylurea (MU), a nonflammable, low-toxicity cosolvent. Leveraging its donor–acceptor amphiphilicity and structural asymmetry, MU enhances miscibility with salt and water, enabling a 2.6 m solution with a distinctive solvation structure: an inner sheath dominated by MU and anions, and an outer layer where water is anchored by MU. This configuration reduces water activity and promotes a robust organic–inorganic interphase, effectively suppressing hydrogen evolution and extending the cathodic stability limit to 1.2 V vs Li<sup>+</sup>/Li. Pouch cells of NbO<sub>2</sub>/LiCoO<sub>2</sub> and NbO<sub>2</sub>/LiMn<sub>2</sub>O<sub>4</sub> show 96% capacity retention after 24 h at 100% state of charge, along with stable cycling over 150 cycles at 0.25 C. This strategy enhances aqueous battery performance while maintaining safety and cost-efficiency, advancing practical implementation.



Driven by the rapid growth of electric vehicles and large-scale energy storage, lithium-ion batteries require continuous advancements in performance and safety.<sup>1</sup> However, commercial nonaqueous lithium-ion electrolytes are flammable, volatile, and toxic, posing serious safety risks.<sup>2,3</sup> Furthermore, their extreme sensitivity to moisture demands manufacturing in costly, energy-intensive dry-room environments. These limitations highlight the urgent need for safer and more cost-effective battery technologies. Aqueous batteries represent a promising alternative, with inherent advantages such as nonflammability, low toxicity, and simplified production.<sup>4–7</sup> Nevertheless, their progress is hindered by the narrow electrochemical stability window of water, which triggers parasitic hydrogen evolution reactions at low potentials. This fundamental constraint restricts the use of high-specific-capacity anode materials and limits the achievable cell voltage.<sup>8,9</sup> Consequently, the energy density of aqueous batteries remains less than one-third of that of nonaqueous lithium-ion batteries, significantly hindering their commercial competitiveness.

Niobium-based oxides are promising anode materials, owing to their three-dimensional tunnel structures and multielectron transfer capability.<sup>10,11</sup> Compared with commonly studied

anode materials for aqueous batteries, such as LiTi<sub>2</sub>(PO<sub>4</sub>)<sub>3</sub> (138 mAh g<sup>-1</sup>, 2.48 V vs Li<sup>+</sup>/Li),<sup>12</sup> Mo<sub>6</sub>S<sub>8</sub> (128 mAh g<sup>-1</sup>, 2.80–2.20 V vs Li<sup>+</sup>/Li),<sup>4</sup> anatase TiO<sub>2</sub> (168 mAh g<sup>-1</sup>, 2.0–1.7 V vs Li<sup>+</sup>/Li),<sup>13</sup> and Li<sub>4</sub>Ti<sub>5</sub>O<sub>12</sub> (175 mAh g<sup>-1</sup>, 1.55 V vs Li<sup>+</sup>/Li),<sup>14,15</sup> niobium-based oxides exhibit low lithium intercalation potentials (2.0–1.0 V vs Li<sup>+</sup>/Li) and exceptionally high theoretical specific capacities (>300 mAh g<sup>-1</sup>). However, this low operating potential also presents a severe challenge for aqueous electrolytes, as it falls outside water's narrow electrochemical stability window. Early studies utilized 21 m LiTFSI in H<sub>2</sub>O electrolytes, but the limited cathodic stability (1.9 V vs Li<sup>+</sup>/Li) restricted the usable capacity to below 80 mAh g<sup>-1</sup>.<sup>16</sup> To improve the performance, dual-salt and ionic liquid systems were introduced to increase the salt concentration (e.g., 50 m LiTFSI + 30 m TMBTFSI in

**Received:** October 14, 2025

**Revised:** November 20, 2025

**Accepted:** December 5, 2025



ACS Publications

© XXXX American Chemical Society

A

<https://doi.org/10.1021/acsenerylett.5c03327>  
ACS Energy Lett. XXXX, XXX, XXX–XXX

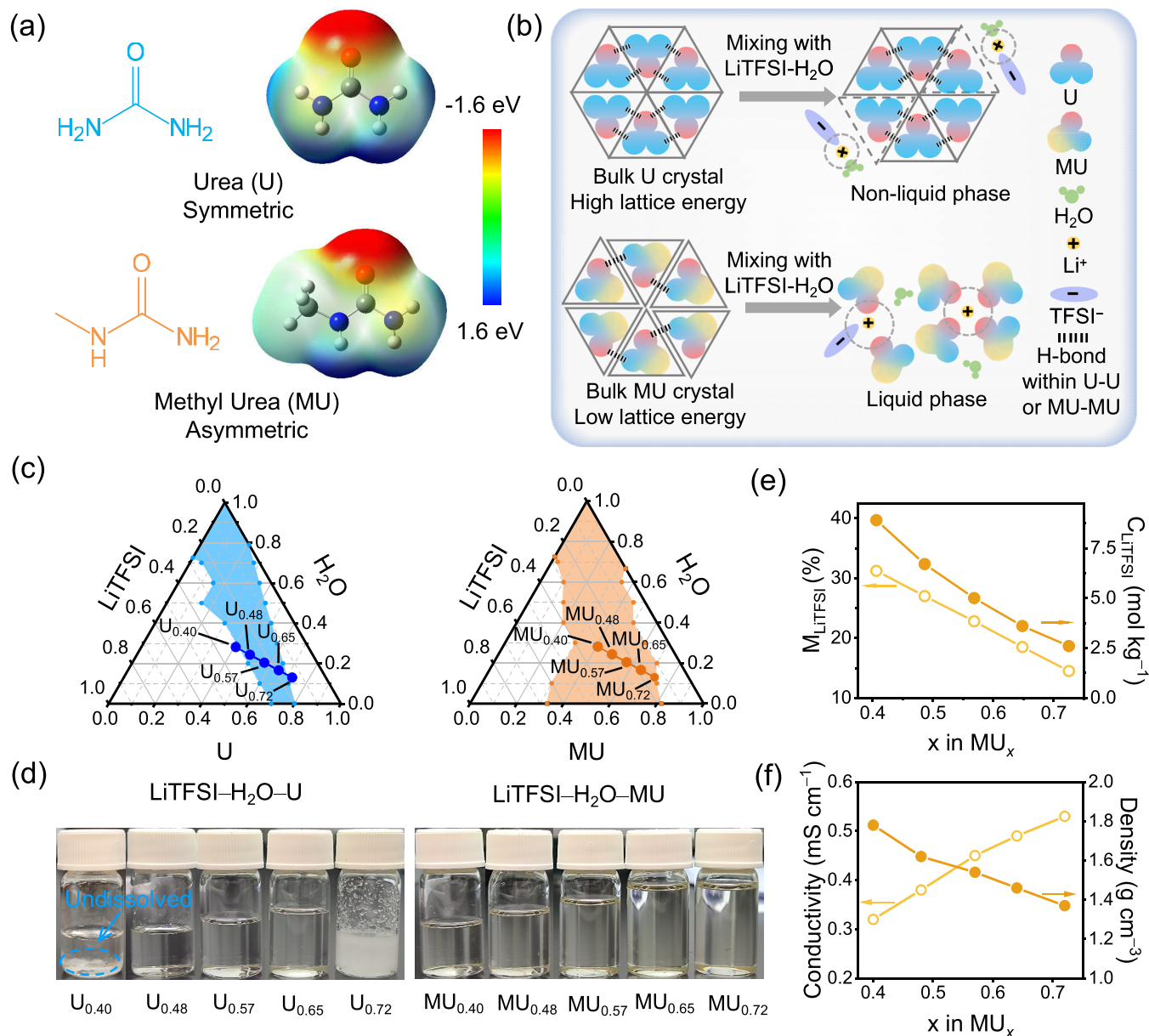


**Figure 1.** Design and characterization of a low-concentration MU-based aqueous electrolyte. (a) Molecular structures and electrostatic potential (ESP) of U and MU. (b) Schematic illustration of dissolution process for LiTFSI-H<sub>2</sub>O-U and LiTFSI-H<sub>2</sub>O-MU ternary systems. The symmetric U molecules form a stable, difficult-to-dissolve crystal, while the asymmetric MU molecules pack loosely, enabling facile dissolution and ion solvation. (c) Ternary phase diagrams for LiTFSI-H<sub>2</sub>O-U and LiTFSI-H<sub>2</sub>O-MU systems based on over 80 samples, showing the significantly broader liquid-phase achieved with MU. (d) Photographs of various electrolytes of U<sub>x</sub> and MU<sub>x</sub> (x is the molar fraction of U or MU in ternary systems). Both high and low salt-concentration U-based systems (U<sub>0.40</sub> and U<sub>0.72</sub>) become immiscible, whereas MU-based systems remain homogeneous. (e) Mole fraction ( $M_{\text{LiTFSI}}$ ) and concentration ( $C_{\text{LiTFSI}}$ ) of LiTFSI in different electrolytes of MU<sub>x</sub>, demonstrating the ability to drastically reduce salt concentration. (f) Key physicochemical properties, including ionic conductivity and density, for the series of MU<sub>x</sub> electrolytes.

H<sub>2</sub>O,<sup>17</sup> 40 m LiTFSI + 20 m EMITFSI in H<sub>2</sub>O<sup>18</sup>), extending the cathodic stability and raising the usable capacity to 200 mAh g<sup>-1</sup>. However, these strategies did not demonstrate a compelling performance advantage over that of the Li<sub>4</sub>Ti<sub>5</sub>O<sub>12</sub> electrode. Moreover, the marginal improvements came at the expense of significantly increased cost, as the use of ultrahigh concentrations of expensive fluorosulfonyl imide salts and/or ionic liquids undermined the fundamental economic benefits of aqueous systems. Despite these efforts, core challenges such as severe self-discharge and capacity degradation remain unresolved, particularly under practical low-rate cycling

conditions, highlighting the persistent issue of parasitic reactions.

To overcome the trade-offs associated with salt-concentrated aqueous electrolytes, we build upon our prior work on a methylurea (MU)-regulated aqueous electrolyte, which features a core-shell solution structure with localized ultrahigh LiTFSI concentration enabled by interactions between MU, LiTFSI, and H<sub>2</sub>O.<sup>19</sup> This system achieved a cathodic stability limit of 1.0 V vs Li<sup>+</sup>/Li and supported stable cycling of high-energy-density rocking-chair NbO<sub>2</sub>/LiMn<sub>2</sub>O<sub>4</sub> full cells (175 Wh kg<sup>-1</sup><sub>cathode+anode</sub>). While our previous 15.9 m electrolyte

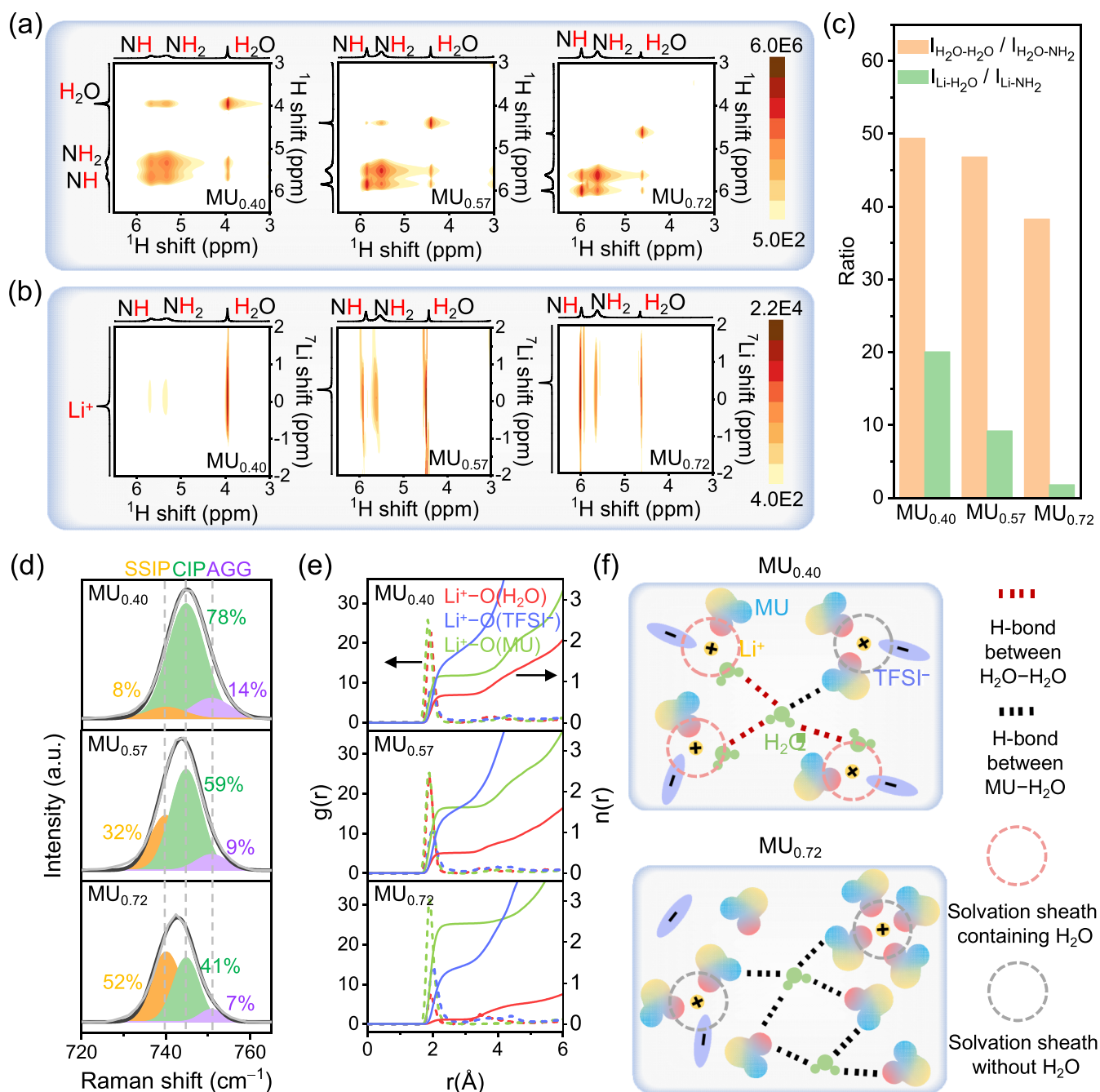


**Figure 2.** 2D-NMR and AIMD analysis of the solvation structure in MU<sub>x</sub> electrolytes. (a) <sup>1</sup>H-<sup>1</sup>H NOESY and (b) <sup>7</sup>Li-<sup>1</sup>H HOESY NMR spectra of the MU<sub>x</sub> electrolytes. (c) Key NMR cross-peak intensity quantifying the changing molecular interactions in MU<sub>x</sub> electrolytes. (d) Raman spectra (S-N-S region) and deconvolution showing the distribution of coordinated TFSI<sup>-</sup> anions. (e) Radial distribution function for Li<sup>+</sup>-solvent pairs calculated from AIMD simulations. (f) Schematic illustrations of solvation structure in MU<sub>0.40</sub> and MU<sub>0.72</sub> electrolytes.

demonstrated the potential of MU, its high salt concentration remained a barrier to practical application. Herein, we shift our electrolyte design from a salt-saturating strategy to a dilute one that leverages the characteristics of structural asymmetry of MU to enhance its miscibility with the LiTFSI salt and water. This approach yields a 2.6 m aqueous electrolyte that not only reduces salt content, viscosity, and density, but also enhances ionic conductivity and broadens the electrochemical stability window to 3.3 V. Unlike conventional 2.6 m aqueous electrolytes dominated by Li<sup>+</sup>(H<sub>2</sub>O)<sub>4</sub> clusters and extensive (H<sub>2</sub>O-H<sub>2</sub>O) hydrogen bond networks, the solvation sheath of MU-regulated electrolyte is restructured owing to the donor-

acceptor amphiphilicity of MU: most H<sub>2</sub>O molecules in the inner solvation sheath are replaced by MU and TFSI<sup>-</sup>, and the excluded H<sub>2</sub>O molecules are anchored by MU, converting H<sub>2</sub>O-H<sub>2</sub>O network into MU-H<sub>2</sub>O interactions. This configuration not only reduces the water activity but also promotes the formation of a robust solid electrolyte interphase (SEI), characterized by an organic-rich outer layer and an inorganic-rich inner layer, extending the cathodic stability limit to 1.2 V vs Li<sup>+</sup>/Li and enabling compatibility with high-specific-capacity NbO<sub>2</sub> anodes. Under rigorous testing conditions (1.65 mAh cm<sup>-2</sup>; P/N = 1.2; 0.25 C; conventional aluminum current collector), rocking-chair NbO<sub>2</sub>/LiCoO<sub>2</sub>



(184 Wh  $\text{kg}_{\text{cathode+anode}}^{-1}$ ) and  $\text{NbO}_2/\text{LiMn}_2\text{O}_4$  (161 Wh  $\text{kg}_{\text{cathode+anode}}^{-1}$ ) pouch cells exhibited 96% capacity retention after 24 h of storage at 100% state of charge (SOC) and stable cycling over 150 cycles. This simple and effective strategy significantly enhances the energy density of aqueous batteries while retaining advantages such as low cost and safety, advancing the practical development of high-voltage aqueous batteries.

**Asymmetric Design Unlocks Dilute Aqueous Electrolytes.** Incorporating organic compounds to reconfigure the solution structure is an effective strategy for widening the electrochemical window of aqueous electrolytes and reducing the cost of high-concentration water-in-salt (WIS) electrolytes.<sup>20–22</sup> Among various reported compounds, urea (U) and MU, both containing dual functional groups  $-\text{C}=\text{O}$  and  $-\text{NH}_2$ , have demonstrated strong capabilities to reduce the activity of water molecules and have been introduced into electrolytes to enhance the electrochemical stability of aqueous systems.<sup>19,23</sup> However, electrolytes based on urea face two critical limitations. First, in the previously reported  $\text{LiTFSI}-\text{H}_2\text{O}-\text{U}$  system, the optimized 4.5 m low-concentration electrolyte exhibits a cathodic stability limit of only 1.5 V vs  $\text{Li}^+/\text{Li}$ , which fails to fully harness the specific capacity advantage of niobium-based oxide anodes. Second, and more critically, urea's physical structure inherently restricts its use in the desired low-salt-concentration regimes. This limitation arises because the high symmetry of urea molecules promotes a tightly packed crystal lattice held by extensive hydrogen bonds. This results in high lattice energy and, consequently, poor solubility, preventing the formation of a homogeneous liquid electrolyte when large proportions of urea are required. In contrast, MU addresses these limitations through a simple yet effective structural modification. The methyl substitution in MU breaks the molecular symmetry. Electrostatic potential (ESP) calculations reveal that the methyl group alters the charge distribution of MU (Figure 1a), disrupting the formation of an ordered MU–MU hydrogen bond network. This leads to looser crystal packing, reduced dissolution energy, and an enhanced ability to solvate cations (Figure 1b). Solubility tests confirmed that the  $\text{LiTFSI}-\text{H}_2\text{O}-\text{MU}$  system has a broader liquid-phase region (Figure 1c). This superior solubility is the key, as it unlocks a vast and previously inaccessible compositional space, making MU an ideal candidate for developing the desired low-salt-concentration aqueous electrolytes.

By gradually introducing U or MU into ca. 1:1  $\text{LiTFSI}/\text{H}_2\text{O}$  mixtures, we prepared electrolytes with varying concentrations, denoted as  $\text{U}_x$  or  $\text{MU}_x$ , where  $x$  represents the mole fraction of U or MU in the solution. Compositions such as  $\text{U}_{0.40}$  and  $\text{U}_{0.72}$ , located outside the liquid-phase region, were immiscible (Figure 1d). In comparison,  $\text{MU}_{0.40}$ ,  $\text{MU}_{0.48}$ ,  $\text{MU}_{0.57}$ ,  $\text{MU}_{0.65}$ , and  $\text{MU}_{0.72}$  remained homogeneous. Therefore, the  $\text{MU}_x$  system was selected for further study to allow flexible tuning of the component ratios to optimize physicochemical properties. The compositions and physicochemical properties of different  $\text{MU}_x$  electrolytes are summarized in Table S1. As shown in Figure 1e, the  $\text{MU}_{0.40}$  sample has a  $\text{LiTFSI}$  mole fraction ( $M_{\text{LiTFSI}}$ ) of 0.31, corresponding to a concentration of 8.9 m ( $\text{mol kg}^{-1}$ ). With increasing MU content, both the mole fraction and the concentration of  $\text{LiTFSI}$  in the solution gradually decrease. At  $\text{MU}_{0.72}$ ,  $M_{\text{LiTFSI}}$  drops by 53% to 0.145, and the salt concentration decreases by 68% to 2.6 m, resulting in a substantial reduction in electrolyte cost compared to

conventional salt-concentrated strategy. Interestingly, the gradual incorporation of solid MU does not degrade the electrolyte's physicochemical properties. The  $\text{MU}_{0.72}$  electrolyte, near the liquid-phase boundary, exhibits optimal values in key parameters such as viscosity (279 mPa·s), conductivity ( $0.53 \text{ mS cm}^{-1}$ ), and density ( $1.37 \text{ g cm}^{-3}$ ) (Table S1 and Figure 1f). Flash point and self-extinguishing time (SET) are two critical parameters for evaluating electrolyte safety. Due to the nonflammable nature of all components, none of the five  $\text{MU}_x$  electrolytes exhibited a detectable flash point within the broad temperature range of 25–300 °C. Furthermore, ignition tests conducted on the  $\text{MU}_{0.72}$  sample demonstrated its nonflammable behavior in a butane–oxygen torch flame, with an SET of  $0 \text{ s g}^{-1}$  (Figure S1). These results confirm that the MU-modulated hybrid electrolyte retains the inherent nonflammable characteristics of aqueous electrolytes.

**Solvation Structure Characterization.** Solution structure profoundly affects the physicochemical and electrochemical properties of the electrolytes. We used two-dimensional nuclear magnetic resonance (2D-NMR) spectroscopy to probe real-time molecular interactions and ab initio molecular dynamics (AIMD) simulations to provide a detailed atomistic picture of the solvation environment in the  $\text{MU}_x$  electrolytes. For the electrolytes of  $\text{MU}_{0.40}$ ,  $\text{MU}_{0.57}$ , and  $\text{MU}_{0.72}$ , both  $^1\text{H}-^1\text{H}$  nuclear Overhauser effect spectroscopy (NOESY) and  $^1\text{H}-^7\text{Li}$  heteronuclear Overhauser effect spectroscopy (HOESY) spectra (Figure 2a and Figure 2b) revealed strong cross-peak signals for  $\text{H}_2\text{O}-\text{NH}/\text{NH}_2$  and  $\text{Li}^+-\text{NH}/\text{NH}_2$ , indicating that MU interacts strongly with both lithium ions and  $\text{H}_2\text{O}$ . As the MU content increases, the  $^1\text{H}$  signal of  $\text{H}_2\text{O}$  shifts downfield, which is attributed to the increased formation of  $\text{H}_2\text{O}-\text{MU}$  hydrogen bonds, reducing the electron density around the protons of water molecules. This observation is supported by two critical quantitative changes. First, there was a gradual decrease in the ratio of  $\text{H}_2\text{O}-\text{H}_2\text{O}$  to  $\text{H}_2\text{O}-\text{NH}_2$  cross-peak intensities ( $I_{\text{H}_2\text{O}-\text{H}_2\text{O}}/I_{\text{H}_2\text{O}-\text{NH}_2}$ , Figure 2c), reflecting a reduction in water–water hydrogen bonds and their replacement mainly by  $\text{H}_2\text{O}-\text{MU}$  hydrogen bonding. Second, the  $\text{Li}-\text{H}_2\text{O}$  to  $\text{Li}-\text{NH}_2$  cross-peak intensity ratio ( $I_{\text{Li}-\text{H}_2\text{O}}/I_{\text{Li}-\text{NH}_2}$ ) also decreases gradually, indicating that continued introduction of MU not only disrupts water–water hydrogen bonds but also displaces water molecules from the solvation sheath. Furthermore, this restructured solvation environment yields another advantage related to anion coordination and the formation of a protective SEI. Raman spectroscopy of the S–N–S bending region ( $730-760 \text{ cm}^{-1}$ , Figure 2d) revealed that even in 2.6 m  $\text{MU}_{0.72}$  electrolyte, approximately 48% of  $\text{TFSI}^-$  remains coordinated with  $\text{Li}^+$ . This high degree of anion coordination would alter the decomposition path of the electrolyte as compared to conventional dilute solution (see discussion below).

These experimental findings are strongly supported by our AIMD simulations, which offer a quantitative atomistic picture of the restructured environment. Radial distribution functions (RDF,  $g(r)$ ) and coordination numbers ( $n(r)$ ) were calculated for  $\text{Li}^+-\text{H}_2\text{O}$ ,  $\text{Li}^+-\text{TFSI}^-$ , and  $\text{Li}^+-\text{MU}$  pairs (Figure 2e), and the inner solvation shell coordination numbers are summarized in Table S2. It is observed that water molecules, MU, and  $\text{TFSI}^-$  all participate in the primary solvation shell of  $\text{Li}^+$ . Compared with  $\text{MU}_{0.40}$  and  $\text{MU}_{0.57}$ , the intensity of the  $\text{H}_2\text{O}$  solvation peak in  $\text{MU}_{0.72}$  decreases significantly. The coordination number of  $\text{H}_2\text{O}$  within the inner solvation sheath



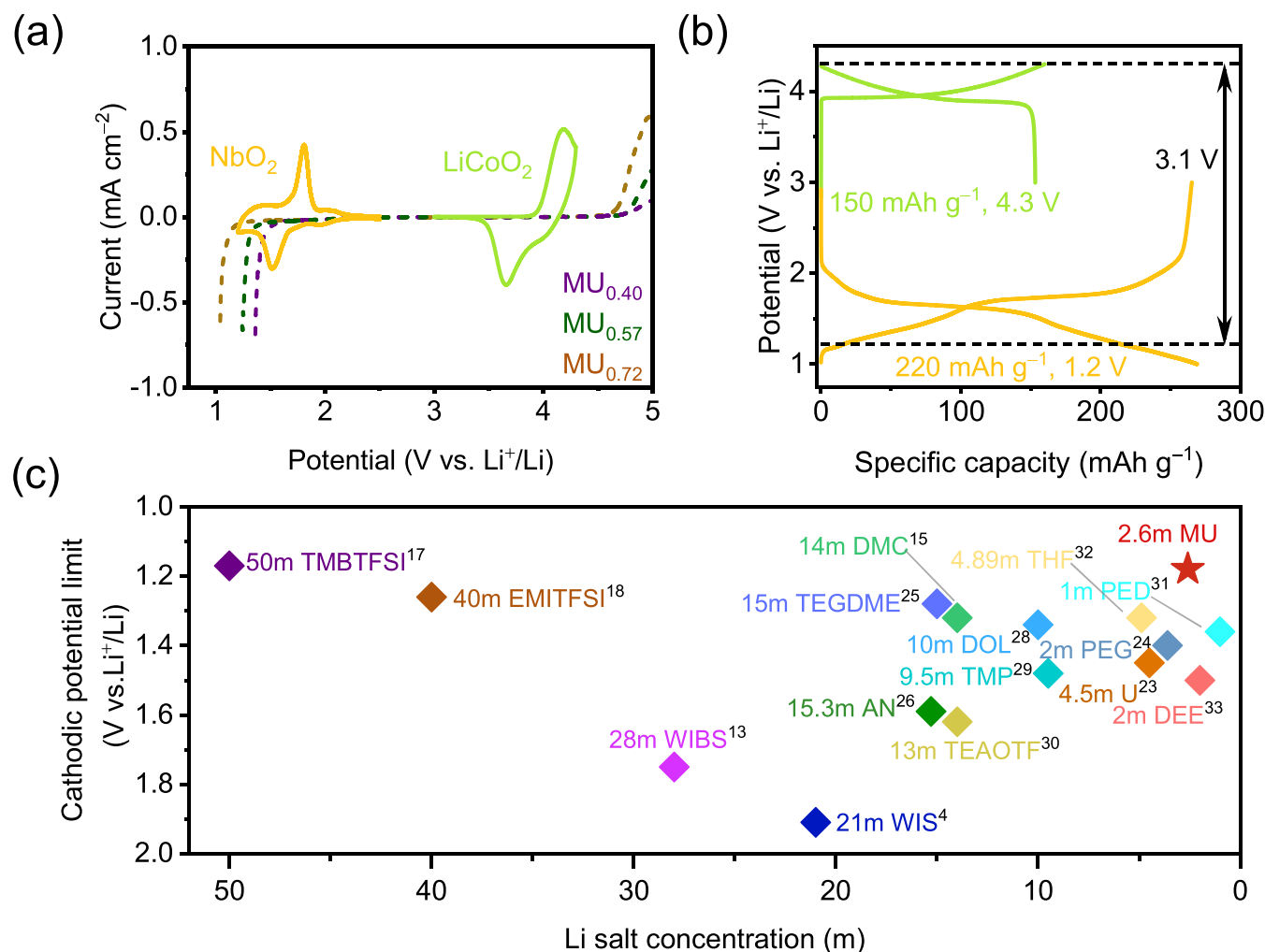
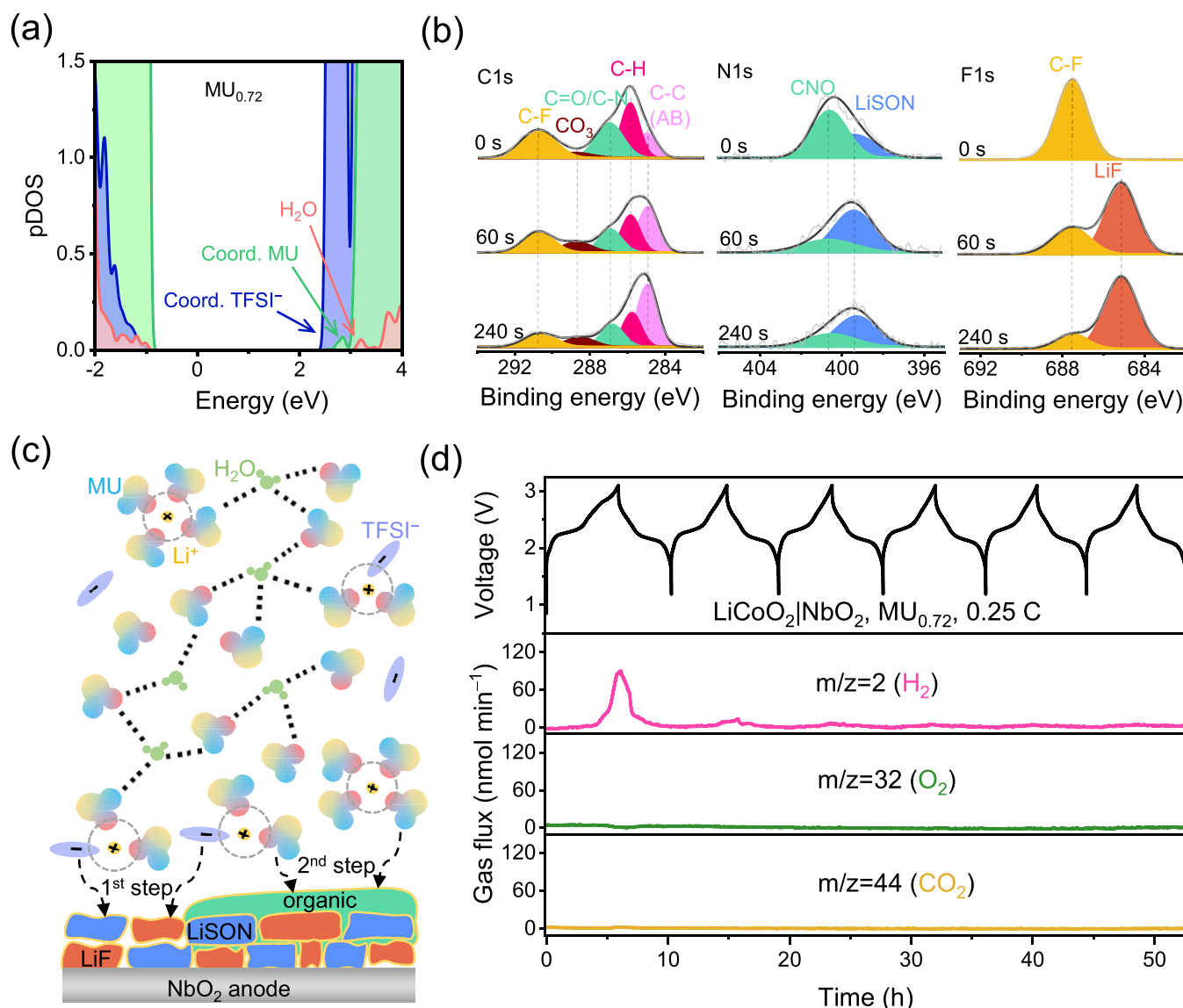


Figure 3. Electrochemical stability window of MU<sub>0.72</sub> (2.6 m). (a) LSV curves on carbon-coated Al electrode in the MU<sub>x</sub> electrolytes, together with CV curves of the NbO<sub>2</sub> and LiCoO<sub>2</sub> electrodes. (b) Potential utilization window of the LiCoO<sub>2</sub> cathode and NbO<sub>2</sub> anode in MU<sub>0.72</sub>. (c) Comparison of cathodic potential limits and lithium salt concentrations across representative aqueous lithium-ion electrolytes.

(at 2.5 Å) drops from 0.67 to 0.1, while the coordination number of TFSI<sup>-</sup> changes only slightly from 1.55 to 1.29. These simulation results are consistent with experimental observations: in MU<sub>0.72</sub>, the primary solvation shell of Li<sup>+</sup> is mainly composed of TFSI<sup>-</sup> and MU, with most H<sub>2</sub>O molecules surrounding the outer layer and being anchored by the left MU (Figure 2f). Notably, MU<sub>0.72</sub> (2.6 m) shows a dramatically different solution structure from the conventional 2.6 m LiTFSI/H<sub>2</sub>O solution (MU<sub>0.00</sub>) that is dominated by Li<sup>+</sup> (H<sub>2</sub>O)<sub>4</sub> clusters and extensive (H<sub>2</sub>O–H<sub>2</sub>O) hydrogen-bond networks (see Figure S2 and Table S2). Hence, this redistribution of water molecules in MU<sub>0.72</sub> leads to disruption of the H<sub>2</sub>O–H<sub>2</sub>O network and a decrease of water activity, which could benefit an expanded electrochemical stability window of MU<sub>0.72</sub>.

**Electrochemical Stability Window.** We carried out linear sweep voltammetry (LSV) measurements to evaluate the electrochemical stability window of the as-prepared electrolytes. The carbon-coated Al foil was used as the working electrode instead of bare Ti because the former is more suitable for practical applications and its larger surface area could enlarge the current density.<sup>19,24</sup> As shown in Figure 3a, the electrochemical stability window of the MU<sub>x</sub> electrolytes indeed progressively expanded with increasing MU content,

reaching up to 3.3 V (1.2–4.5 V vs Li<sup>+</sup>/Li) for MU<sub>0.72</sub>. This enhancement was accompanied by a downward shift in the cathodic onset potential, from 1.6 V in MU<sub>0.40</sub> to 1.2 V in MU<sub>0.72</sub> vs Li<sup>+</sup>/Li (Figure 3a). Characteristic peaks in the cyclic voltammetry (CV) data further confirmed that the MU<sub>0.72</sub> electrolyte supports reversible lithium insertion and extraction in both NbO<sub>2</sub> and LiCoO<sub>2</sub> electrodes. Accordingly, a full rocking-chair lithium-ion cell using NbO<sub>2</sub> as the anode and LiCoO<sub>2</sub> as the cathode could achieve a high cutoff voltage of 3.1 V and a high theoretical energy density of approximately 200 Wh kg<sup>-1</sup><sub>cathode+anode</sub> (Figure 3b). To enable a direct comparison with previously reported representative aqueous electrolytes, we performed LSV measurements on those electrolytes under identical conditions (Figure S3). Notably, MU<sub>0.72</sub> demonstrated a lower cathodic limit than most reported aqueous electrolytes based on salt-concentrated or water–organic hybrid strategies.<sup>4,13,15,17,23–33</sup> Its performance even approached that of ultrahigh-concentration lithium salt–ionic liquid electrolyte (e.g., 50 m LiTFSI + 30 m TMBTFSI in H<sub>2</sub>O) (Figure 3c), while using significantly less lithium salt. Therefore, compared with previous reports utilizing niobium-based oxides as anodes, our approach offers multiple advantages, including a lower lithiation potential, higher



**Figure 4.** Understanding and characterization of  $\text{MU}_{0.72}$  derived SEI. (a) Calculated pDOS for the  $\text{MU}_{0.72}$  electrolyte components, predicting that TFSI $^-$  anions and MU molecules will be preferentially reduced over water. (b) XPS depth-profiling of the  $\text{NbO}_2$  anode after cycling. The spectra confirm the formation of a dual-layer SEI with an inorganic-rich inner layer and an organic-rich outer layer. AB stands for acetylene black. (c) Schematic illustration of the SEI formation on the  $\text{NbO}_2$  anode surface. The initially preferential reduction of TFSI $^-$  leads to the formation of the inorganic-rich inner layer, while the subsequent reduction of MU results in the formation of the organic-rich outer layer. (d) In-situ DEMS analysis of the  $\text{LiCoO}_2|\text{NbO}_2$  full cell using the  $\text{MU}_{0.72}$  electrolyte during cycling.

specific capacity, and substantially reduced salt concentration (Table S3).

**Interphase Formation and Characterization.** The electrochemical stability window of electrolyte is widely reported to be associated with either the solution structure<sup>24,31</sup> or the SEI<sup>34</sup> or both.<sup>4,21,23,32</sup> To understand the broadened electrochemical stability window of  $\text{MU}_{0.72}$ , we investigated the lowest unoccupied molecular orbital (LUMO) based on its solution structure and characterized the composition and configuration of its derived SEI. The projected density of states (pDOS) for the 2.6 m low-concentration  $\text{MU}_{0.72}$  electrolyte is shown in Figure 4a and Figure S4. The LUMO of the solution is primarily composed of contributions from TFSI $^-$ , followed by contributions from MU and  $\text{H}_2\text{O}$  at progressively higher energy levels. This energy alignment suggests that during reduction TFSI $^-$  and MU will decompose preferentially over  $\text{H}_2\text{O}$ . As a result,  $\text{H}_2\text{O}$  remains reductively stable, while the

decomposition of TFSI $^-$  and MU generates passivation products that further prevent the electrolyte from decomposition on the  $\text{NbO}_2$  surface, both of which contribute to the broader electrochemical stability window observed in  $\text{MU}_{0.72}$ .

To investigate the SEI on the  $\text{NbO}_2$  anode, we conducted X-ray photoelectron spectroscopy (XPS) analysis. As shown in Figure 4b, the spectra reveal the presence of MU-derived organic species (C–H, C–N, and C=O in the C 1s region; CNO in N 1s), and TFSI $^-$ -derived inorganic species such as LiF and lithium sulfur oxynitride (LiSON). With progressive Ar $^+$  sputtering, the intensities of the CNO and C–H species decrease, while the signals for LiF and LiSON become significantly more prominent. These depth-dependent changes indicate that, despite the low lithium salt concentration, the high degree of TFSI $^-$  and MU coordination in the solvation structure of  $\text{MU}_{0.72}$  promotes successive decomposition of TFSI $^-$  and MU to form a dual-layered SEI that is organically

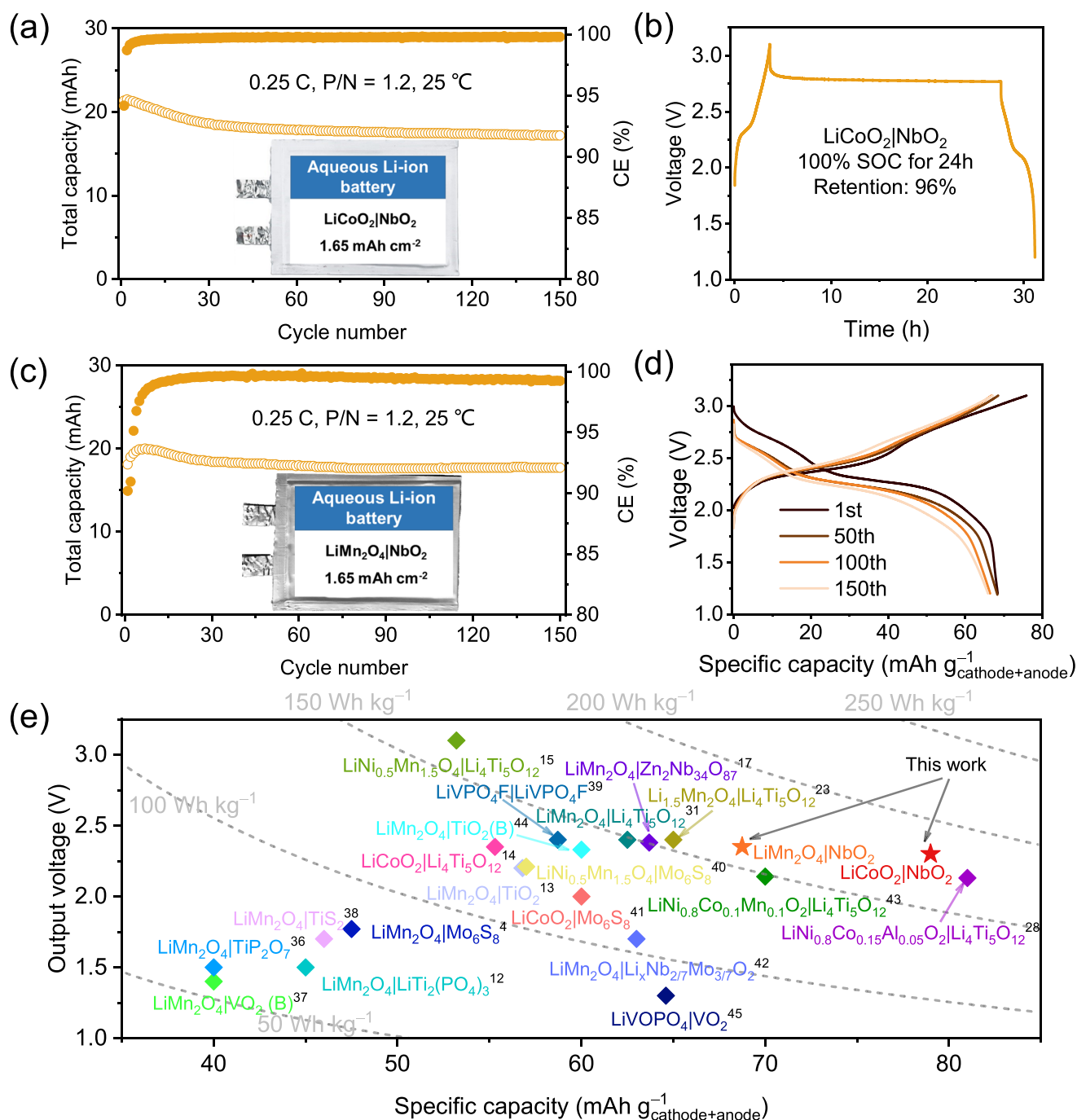


Figure 5. Electrochemical performances of aqueous pouch cells using  $\text{NbO}_2$  anode and  $\text{MU}_{0.72}$  electrolyte. (a) Cycling performance and (b) self-discharge behavior of the  $\text{LiCoO}_2|\text{NbO}_2$  pouch cell. (c) Cycling performance and (d) charge-discharge profiles of the  $\text{LiMn}_2\text{O}_4|\text{NbO}_2$  pouch cell. (e) Comparison of energy density for representative aqueous lithium-ion batteries.

rich on the surface and inorganic-rich beneath. This SEI formation is schematically illustrated in Figure 4c, consistent with the simulation results, as shown in Figure 4a.

In-situ differential electrochemical mass spectrometry measurement (DEMS) was further employed to monitor gaseous products during full-cell operation, providing direct evidence of the SEI's effectiveness in suppressing side reactions between the electrolyte and electrodes. As shown in Figure 4d, no significant  $\text{O}_2$  or  $\text{CO}_2$  signals were detected throughout the entire testing process. In contrast, a significant  $\text{H}_2$  signal emerged during the first charge cycle when the voltage exceeded over 2.7 V. However, in the second cycle, the  $\text{H}_2$

signal intensity decreased dramatically, and from the third to sixth cycles, no detectable gas evolution was observed. Combining the results from both mass spectrometry and XPS, it is deduced that the initial formation of TFSI<sup>-</sup>-derived inorganic-rich SEI is insufficient to suppress the hydrogen evolution reaction (HER) completely; the following addition of MU-derived organic-rich SEI may become necessary to compact the SEI and prevent HER more efficiently. These findings highlight that SEI engineering through solvation structure design is as crucial as water activity modulation. The combined effect of low water activity and a robust SEI provides



synergistic thermodynamic and kinetic suppression of the HER.

**High-Energy-Density Aqueous Pouch Cells.** The aforementioned results clearly demonstrate that the MU<sub>0.72</sub> aqueous electrolyte, with a low salt concentration of 2.6 m, significantly extends the cathodic stability limit to 1.2 V vs Li<sup>+</sup>/Li, with HER effectively suppressed during cycling. To evaluate the long-term cycling compatibility of the as-prepared MU<sub>x</sub> electrolytes with the NbO<sub>2</sub> anode under practical conditions, we assembled LiCoO<sub>2</sub>/NbO<sub>2</sub> pouch cells using 3.5 × 4.7 cm LiCoO<sub>2</sub> cathodes (~12.0 mg cm<sup>-2</sup>) and NbO<sub>2</sub> anodes (~6.7 mg cm<sup>-2</sup>), both supported on aluminum current collectors. The positive-to-negative electrode capacity ratio (P/N) was maintained at ~1.2. The pouch cells were fabricated in an ambient atmosphere without moisture control.

As shown in Figure 5a and Figure S5, under stringent testing conditions of a small rate of 0.25 C, the LiCoO<sub>2</sub>/NbO<sub>2</sub> pouch cell employing the MU<sub>0.72</sub> electrolyte delivered a high initial Coulombic efficiency of ~93% and a reversible capacity of ~79 mAh g<sup>-1</sup><sub>cathode+anode</sub> (based on the total mass of cathode and anode materials). The cell retained 80% of its initial capacity after 150 cycles, with an average Coulombic efficiency of 99.8%, demonstrating excellent cycling stability. Furthermore, this battery exhibited strong self-discharge resistance (Figure 5b), retaining 96% of its capacity after 24 h at 100% SOC, confirming the minimal occurrence of side reactions under these harsh conditions. In contrast, cells using MU<sub>0.40</sub> and MU<sub>0.57</sub> electrolytes showed significantly lower initial Coulombic efficiencies of 55.8% and 78.9%, respectively, and their capacities dropped below 70% within the first 10 cycles, indicating poor compatibility with the low-potential NbO<sub>2</sub> anode (Figure S5).

Considering the low cost and stable spinel structure of LiMn<sub>2</sub>O<sub>4</sub>, we further assembled LiMn<sub>2</sub>O<sub>4</sub>/NbO<sub>2</sub> pouch cells for comparison. As shown in Figures 5c and 5d, the MU<sub>0.72</sub>-based LiMn<sub>2</sub>O<sub>4</sub>/NbO<sub>2</sub> cell exhibited a high capacity retention of 88.5% over 150 cycles at 0.25 C, further confirming the robustness of the MU<sub>0.72</sub> electrolyte across different battery chemistries. In terms of energy density, our fabricated LiCoO<sub>2</sub>/NbO<sub>2</sub> and LiMn<sub>2</sub>O<sub>4</sub>/NbO<sub>2</sub> pouch cells achieved gravimetric energy densities of ~184 and ~161 Wh kg<sup>-1</sup><sub>cathode+anode</sub>, respectively, outperforming previously reported aqueous batteries<sup>4,12,14,35–45</sup> (Figure 5e and Table S4). Importantly, these results were achieved using a 2.6 m MU-modulated aqueous electrolyte without compromising cost-effectiveness or safety, underscoring the potential of our electrolyte design for practical applications in high-voltage aqueous lithium-ion batteries.

In summary, we present a simple yet effective diluting electrolyte strategy for the development of high-voltage aqueous batteries. By leveraging the structural asymmetry of MU, we accessed a previously unexplored compositional space of low-salt concentration LiTFSI–H<sub>2</sub>O–MU electrolytes, which is inaccessible for the LiTFSI–H<sub>2</sub>O–U electrolytes using symmetric urea. Within this uncharted regime, the solvation structure can be further tuned by adjusting the MU content, taking advantage of its donor–acceptor amphiphilicity. This property enables simultaneous modulation of the inner solvation sheath and anchoring of water molecules in the outer coordination layer. As a result, we developed a 2.6 m aqueous electrolyte with suppressed water activity and the ability to form a stable organic–inorganic dual-layer interphase. This interphase effectively mitigates parasitic

hydrogen evolution, extending the cathodic stability limit to 1.2 V vs Li<sup>+</sup>/Li and enabling compatibility with low-potential, high-capacity NbO<sub>2</sub> anode. Under stringent testing conditions (P/N ratio = 1.2; Al current collectors), NbO<sub>2</sub>/LiCoO<sub>2</sub> (184 Wh kg<sup>-1</sup><sub>cathode+anode</sub>) and NbO<sub>2</sub>/LiMn<sub>2</sub>O<sub>4</sub> (161 Wh kg<sup>-1</sup><sub>cathode+anode</sub>) pouch cells demonstrated 96% capacity retention after 24 h at 100% SOC and stable cycling over 150 cycles, even at a low rate of 0.25 C. This diluting electrolyte strategy reduces salt concentration, viscosity, and density while simultaneously enhancing ionic conductivity and broadening the electrochemical stability window. Consequently, it significantly enhances the energy density of aqueous batteries without compromising cost-effectiveness or safety, thereby promoting their practical advancement.

## ■ ASSOCIATED CONTENT

### Supporting Information

The Supporting Information is available free of charge at <https://pubs.acs.org/doi/10.1021/acsenergylett.5c03327>.

Experimental methods regarding electrolyte and electrode preparation, CV, LSV, Raman, 2D-NMR, ionic conductivity and viscosity measurements for electrolytes, XPS, in-suit DEMS measurements, and computational details (PDF)

## ■ AUTHOR INFORMATION

### Corresponding Authors

Shi Liu – Research Center for Industries of the Future and Department of Physics, School of Science, Westlake University, Hangzhou 310030, China; Institute of Natural Sciences, Westlake Institute for Advanced Study, Hangzhou 310024, China; [orcid.org/0000-0002-8488-4848](https://orcid.org/0000-0002-8488-4848); Email: [liushi@westlake.edu.cn](mailto:liushi@westlake.edu.cn)

Jianhui Wang – Division of Solar Energy Conversion and Catalysis at Westlake University, Zhejiang Baima Lake laboratory Co. Ltd., Hangzhou 310000, China; Zhejiang Key Laboratory of 3D Micro/Nano Fabrication and Characterization, Department of Electronic and Information Engineering, School of Engineering and Research Center for Industries of the Future, Westlake University, Hangzhou 310030, China; Institute of Advanced Technology, Westlake Institute for Advanced Study, Hangzhou 310024, China; [orcid.org/0000-0002-4170-1132](https://orcid.org/0000-0002-4170-1132); Email: [wangjianhui@westlake.edu.cn](mailto:wangjianhui@westlake.edu.cn)

### Authors

Chuanyu Hou – School of Materials Science & Engineering, Zhejiang University, Hangzhou 310024 Zhejiang, China; Zhejiang Key Laboratory of 3D Micro/Nano Fabrication and Characterization, Department of Electronic and Information Engineering, School of Engineering and Research Center for Industries of the Future, Westlake University, Hangzhou 310030, China; Institute of Advanced Technology, Westlake Institute for Advanced Study, Hangzhou 310024, China

Changming Ke – Department of Physics, School of Science, Westlake University, Hangzhou 310030, China; Institute of Natural Sciences, Westlake Institute for Advanced Study, Hangzhou 310024, China

Runze Chen – School of Materials Science & Engineering, Zhejiang University, Hangzhou 310024 Zhejiang, China; Zhejiang Key Laboratory of 3D Micro/Nano Fabrication

and Characterization, Department of Electronic and Information Engineering, School of Engineering and Research Center for Industries of the Future, Westlake University, Hangzhou 310030, China; Institute of Advanced Technology, Westlake Institute for Advanced Study, Hangzhou 310024, China

**Yangfan Lin** – Zhejiang Key Laboratory of 3D Micro/Nano Fabrication and Characterization, Department of Electronic and Information Engineering, School of Engineering and Research Center for Industries of the Future, Westlake University, Hangzhou 310030, China; Institute of Advanced Technology, Westlake Institute for Advanced Study, Hangzhou 310024, China; [orcid.org/0000-0003-2297-4124](https://orcid.org/0000-0003-2297-4124)

**Qin Huang** – Zhejiang Key Laboratory of 3D Micro/Nano Fabrication and Characterization, Department of Electronic and Information Engineering, School of Engineering and Research Center for Industries of the Future, Westlake University, Hangzhou 310030, China; Institute of Advanced Technology, Westlake Institute for Advanced Study, Hangzhou 310024, China

Complete contact information is available at:

<https://pubs.acs.org/10.1021/acsenerylett.5c03327>

## Author Contributions

J.W. and C.H. designed the experiments. C.H. carried out electrolyte preparation, solution structure characterizations and electrochemical performances. C.K. and S.L. designed and performed the AIMD simulations. All authors contributed to the data analysis and manuscript preparation. J.W. conceived and led the project. C.H. and C.K. contributed equally to this work.

## Notes

The authors declare no competing financial interest.

## ACKNOWLEDGMENTS

This work was supported by Zhejiang Baima Lake Laboratory Co. Ltd., Zhejiang Key Laboratory of 3D Micro/Nano Fabrication and Characterization, Research Center for Industries of the Future (RCIF), Westlake Education Foundation, National Natural Science Foundation of China (Grant No. 21975207) and Zhejiang Provincial Natural Science Foundation of China (LR25A040004). The computational resource is provided by the Open Source Supercomputing Center of S-A-I.

## REFERENCES

- (1) Armand, M.; Tarascon, J. M. Building Better Batteries. *Nature* **2008**, *451* (7179), 652–657.
- (2) Xu, K. Nonaqueous Liquid Electrolytes for Lithium-Based Rechargeable Batteries. *Chem. Rev.* **2004**, *104* (10), 4303–4418.
- (3) Yamada, Y.; Wang, J.; Ko, S.; Watanabe, E.; Yamada, A. Advances and Issues in Developing Salt-Concentrated Battery Electrolytes. *Nat. Energy* **2019**, *4* (4), 269–280.
- (4) Suo, L.; Borodin, O.; Gao, T.; Olguin, M.; Ho, J.; Fan, X.; Luo, C.; Wang, C.; Xu, K. “Water-in-salt” Electrolyte Enables High-Voltage Aqueous Lithium-ion Chemistries. *Science* **2015**, *350* (6263), 938–943.
- (5) Kim, H.; Hong, J.; Park, K.-Y.; Kim, H.; Kim, S.-W.; Kang, K. Aqueous Rechargeable Li and Na Ion Batteries. *Chem. Rev.* **2014**, *114* (23), 11788–11827.
- (6) Liang, G.; Mo, F.; Ji, X.; Zhi, C. Non-metallic Charge Carriers for Aqueous Batteries. *Nat. Rev. Mater.* **2021**, *6* (2), 109–123.

- (7) Zhang, F.; Zhang, W.; Wexler, D.; Guo, Z. Recent Progress and Future Advances on Aqueous Monovalent-Ion Batteries towards Safe and High-Power Energy Storage. *Adv. Mater.* **2022**, *34* (24), No. 2107965.
- (8) Liang, Y.; Yao, Y. Designing Modern Aqueous Batteries. *Nat. Rev. Mater.* **2023**, *8* (2), 109–122.
- (9) Zhang, H.; Liu, X.; Li, H.; Hasa, I.; Passerini, S. Challenges and Strategies for High-Energy Aqueous Electrolyte Rechargeable Batteries. *Angew. Chem., Int. Ed.* **2021**, *60* (2), 598–616.
- (10) Griffith, K. J.; Wiaderek, K. M.; Cibil, G.; Marbella, L. E.; Grey, C. P. Niobium Tungsten Oxides for High-Rate Lithium-Ion Energy Storage. *Nature* **2018**, *559* (7715), 556–563.
- (11) Yang, Y.; Zhao, J. Wadsley–Roth Crystallographic Shear Structure Niobium-Based Oxides: Promising Anode Materials for High-Safety Lithium-Ion Batteries. *Adv. Sci.* **2021**, *8* (12), No. 2004855.
- (12) Luo, J.-Y.; Cui, W.-J.; He, P.; Xia, Y.-Y. Raising the Cycling Stability of Aqueous Lithium-Ion Batteries by Eliminating Oxygen in the Electrolyte. *Nat. Chem.* **2010**, *2* (9), 760–765.
- (13) Suo, L.; Borodin, O.; Sun, W.; Fan, X.; Yang, C.; Wang, F.; Gao, T.; Ma, Z.; Schroeder, M.; von Cresce, A.; et al. Advanced High-Voltage Aqueous Lithium-Ion Battery Enabled by “Water-in-Bisalt” Electrolyte. *Angew. Chem., Int. Ed.* **2016**, *55* (25), 7136–7141.
- (14) Yamada, Y.; Usui, K.; Sodeyama, K.; Ko, S.; Tateyama, Y.; Yamada, A. Hydrate-Melt Electrolytes for High-Energy-Density Aqueous Batteries. *Nat. Energy* **2016**, *1* (10), No. 16129.
- (15) Wang, F.; Borodin, O.; Ding, M. S.; Gobet, M.; Vatamanu, J.; Fan, X.; Gao, T.; Eidson, N.; Liang, Y.; Sun, W.; et al. Hybrid Aqueous/Non-aqueous Electrolyte for Safe and High-Energy Li-Ion Batteries. *Joule* **2018**, *2* (5), 927–937.
- (16) Lakhnot, A. S.; Gupta, T.; Singh, Y.; Hundekar, P.; Jain, R.; Han, F.; Koratkar, N. Aqueous Lithium-Ion Batteries with Niobium Tungsten Oxide Anodes for Superior Volumetric and Rate Capability. *Energy Storage Mater.* **2020**, *27*, 506–513.
- (17) Zhu, X.; Mao, M.; Lin, Z.; Yue, J.; Li, M.; Lv, T.; Zhou, A.; Hu, Y.-S.; Li, H.; Huang, X.; et al. Wadsley–Roth Phase Niobium-Based Oxide Anode Promising High Power and Energy Density Aqueous Li-Ion Batteries. *ACS Mater. Lett.* **2022**, *4*, 1574–1583.
- (18) Becker, M.; Bernasconi, F.; Egorov, K.; Svaluto-Ferro, E.; Kühnel, R.-S.; Battaglia, C. J. E. S. M. Niobium Oxide Anode Materials with Suppressed Activity Toward Hydrogen Evolution Reaction for Aqueous Batteries. *Energy Storage Mater.* **2024**, *71*, No. 103613.
- (19) Lin, R.; Ke, C.; Chen, J.; Liu, S.; Wang, J. Asymmetric Donor-Acceptor Molecule-Regulated Core-Shell-Solvation Electrolyte for High-Voltage Aqueous Batteries. *Joule* **2022**, *6* (2), 399–417.
- (20) Zhou, L.; Tian, S.; Du, X.; Liu, T.; Zhang, H.; Zhang, J.; Hu, S.; Chen, Z.; Zhang, J.; Cui, G. Suppressing Hydrogen Evolution in Aqueous Lithium-Ion Batteries with Double-Site Hydrogen Bonding. *ACS Energy Lett.* **2023**, *8* (1), 40–47.
- (21) Jeong, I.; Kim, S.; Kim, Y.; Kim, C.; Kang, J.; Ha, J. H.; Cho, Y.; Kang, S. J.; Ryu, J.; Han, J. W.; et al. Toward Long-Life High-Voltage Aqueous Li-Ion Batteries: from Solvation Chemistry to Solid-Electrolyte-Interphase Layer Optimization Against Electron Tunneling Effect. *Adv. Mater.* **2025**, *37* (6), No. 2412652.
- (22) Shang, Y.; Chen, N.; Li, Y.; Chen, S.; Li, Z.; Li, S.; Ren, X.; Ye, Y.; Li, L.; Wu, F.; et al. Tiny-Ligand Solvation Electrolyte Enabled Fast-Charging Aqueous Batteries. *Angew. Chem., Int. Ed.* **2025**, *64* (14), No. e202423808.
- (23) Xu, J.; Ji, X.; Zhang, J.; Yang, C.; Wang, P.; Liu, S.; Ludwig, K.; Chen, F.; Kofinas, P.; Wang, C. Aqueous Electrolyte Design for Super-Stable 2.5 V LiMn<sub>2</sub>O<sub>4</sub> || Li<sub>4</sub>Ti<sub>5</sub>O<sub>12</sub> Pouch Cells. *Nat. Energy* **2022**, *7* (2), 186–193.
- (24) Xie, J.; Liang, Z.; Lu, Y. C. Molecular Crowding Electrolytes for High-Voltage Aqueous Batteries. *Nat. Mater.* **2020**, *19* (9), 1006–1011.
- (25) Shang, Y.; Chen, N.; Li, Y.; Chen, S.; Lai, J.; Huang, Y.; Qu, W.; Wu, F.; Chen, R. An “Ether-In-Water” Electrolyte Boosts Stable

Interfacial Chemistry for Aqueous Lithium-Ion Batteries. *Adv. Mater.* **2020**, *32* (40), No. 2004017.

(26) Chen, J.; Vatamanu, J.; Xing, L.; Borodin, O.; Chen, H.; Guan, X.; Liu, X.; Xu, K.; Li, W. Improving Electrochemical Stability and Low-Temperature Performance with Water/Acetonitrile Hybrid Electrolytes. *Adv. Energy Mater.* **2020**, *10* (3), No. 1902654.

(27) Becker, M.; Rentsch, D.; Reber, D.; Aribia, A.; Battaglia, C.; Kühnel, R.-S. The Hydrotropic Effect of Ionic Liquids in Water-in-Salt Electrolytes. *Angew. Chem., Int. Ed.* **2021**, *60* (25), 14100–14108.

(28) Ma, Z.; Chen, J.; Vatamanu, J.; Borodin, O.; Bedrov, D.; Zhou, X.; Zhang, W.; Li, W.; Xu, K.; Xing, L. Expanding the Low-Temperature and High-Voltage Limits of Aqueous Lithium-Ion Battery. *Energy Storage Mater.* **2022**, *45*, 903–910.

(29) Li, Q.; Yang, C.; Zhang, J.; Ji, X.; Xu, J.; He, X.; Chen, L.; Hou, S.; Uddin, J.; Addison, D.; et al. Controlling Intermolecular Interaction and Interphase Chemistry Enabled Sustainable Water-tolerance  $\text{LiMn}_2\text{O}_4\|\text{Li}_4\text{Ti}_5\text{O}_{12}$  Batteries. *Angew. Chem., Int. Ed.* **2022**, *61* (49), No. e202214126.

(30) Zhou, A.; Zhang, J.; Chen, M.; Yue, J.; Lv, T.; Liu, B.; Zhu, X.; Qin, K.; Feng, G.; Suo, L. An Electric-Field-Reinforced Hydrophobic Cationic Sieve Lowers the Concentration Threshold of Water-In-Salt Electrolytes. *Adv. Mater.* **2022**, *34* (47), No. 2207040.

(31) Lin, R.; Chen, J.; Ke, C.; Liu, S.; Wang, J. A Dilute Fluorine-Free Electrolyte Design for High-Voltage Hybrid Aqueous Batteries. *J. Energy Chem.* **2023**, *77*, 180–190.

(32) Zhang, C.; Chen, B.; Chen, Q.; Liu, Y.; Kong, X.; Suo, L.; Lu, J.; Pan, H. Regulation of Molecular Microheterogeneity in Electrolytes Enables Ampere-Hour-Level Aqueous  $\text{LiMn}_2\text{O}_4\|\text{Li}_4\text{Ti}_5\text{O}_{12}$  Pouch Cells. *Adv. Mater.* **2024**, *36* (40), No. 2405913.

(33) Zhang, C.; Chen, B.; Chen, Q.; Tian, C.; Zhou, M.; Zhao, X.; Li, Z.; Fan, L.; Kong, X.; Pan, H. Microstructure Design of Electrolytes for High-Energy-Density Aqueous Batteries. *ACS Energy Lett.* **2024**, *9* (9), 4691–4698.

(34) Zhu, X.; Lin, Z.; Lai, J.; Lv, T.; Lin, T.; Pan, H.; Feng, J.; Wang, Q.; Han, S.; Chen, R.; et al. Highly Efficient Spatially-Temporally Synchronized Construction of Robust  $\text{Li}_3\text{PO}_4$ -rich Solid-Electrolyte Interphases in Aqueous Li-ion Batteries. *Angew. Chem., Int. Ed.* **2024**, *63* (5), No. e202317549.

(35) Suo, L.; Borodin, O.; Sun, W.; Fan, X.; Yang, C.; Wang, F.; Gao, T.; Ma, Z.; Schroeder, M.; von Cresce, A.; et al. Advanced High-Voltage Aqueous Lithium-Ion Battery Enabled by "Water-in-Bisalt" Electrolyte. *Angew. Chem., Int. Ed.* **2016**, *55* (25), 7136–7141.

(36) Wen, Y.; Chen, L.; Pang, Y.; Guo, Z.; Bin, D.; Wang, Y.-g.; Wang, C.; Xia, Y.  $\text{TiP}_2\text{O}_7$  and Expanded Graphite Nanocomposite as Anode Material for Aqueous Lithium-Ion Batteries. *ACS Appl. Mater.* **2017**, *9* (9), 8075–8082.

(37) Ni, J.; Jiang, W.; Yu, K.; Gao, Y.; Zhu, Z. Hydrothermal synthesis of  $\text{VO}_2$  (B) Nanostructures and Application in Aqueous Li-Ion Battery. *Electrochim. Acta* **2011**, *56* (5), 2122–2126.

(38) Sun, W.; Suo, L.; Wang, F.; Eidson, N.; Yang, C.; Han, F.; Ma, Z.; Gao, T.; Zhu, M.; Wang, C. "Water-in-Salt" Electrolyte Enabled  $\text{LiMn}_2\text{O}_4/\text{TiS}_2$  Lithium-Ion Batteries. *Electrochem. Commun.* **2017**, *82*, 71–74.

(39) Yang, C.; Ji, X.; Fan, X.; Gao, T.; Suo, L.; Wang, F.; Sun, W.; Chen, J.; Chen, L.; Han, F.; et al. Flexible Aqueous Li-Ion Battery with High Energy and Power Densities. *Adv. Mater.* **2017**, *29* (44), No. 1701972.

(40) Wang, F.; Suo, L.; Liang, Y.; Yang, C.; Han, F.; Gao, T.; Sun, W.; Wang, C. Spinel  $\text{LiNi}_{0.5}\text{Mn}_{1.5}\text{O}_4$  Cathode for High-Energy Aqueous Lithium-Ion Batteries. *Adv. Energy Mater.* **2017**, *7* (8), No. 1600922.

(41) Wang, F.; Lin, Y.; Suo, L.; Fan, X.; Gao, T.; Yang, C.; Han, F.; Qi, Y.; Xu, K.; Wang, C. Stabilizing High Voltage  $\text{LiCoO}_2$  Cathode in Aqueous Electrolyte with Interphase-Forming Additive. *Energy Environ. Sci.* **2016**, *9* (12), 3666–3673.

(42) Yun, J.; Sagehashi, R.; Sato, Y.; Masuda, T.; Hoshino, S.; Rajendra, H. B.; Okuno, K.; Hosoe, A.; Bandarenka, A. S.; Yabuuchi, N. Nanosized and Metastable Molybdenum Oxides as Negative Electrode Materials for Durable High-Energy Aqueous Li-Ion

Batteries. *Proc. Natl. Acad. Sci. U. S. A.* **2021**, *118* (48), No. e2024969118.

(43) Reber, D.; Borodin, O.; Becker, M.; Rentsch, D.; Thienenkamp, J. H.; Grissa, R.; Zhao, W.; Aribia, A.; Brunklaus, G.; Battaglia, C.; et al. Water/Ionic Liquid/Succinonitrile Hybrid Electrolytes for Aqueous Batteries. *Adv. Funct. Mater.* **2022**, *32* (20), No. 2112138.

(44) Zhou, A.; Liu, Y.; Zhu, X.; Li, X.; Yue, J.; Ma, X.; Gu, L.; Hu, Y.-S.; Li, H.; Huang, X.; et al.  $\text{TiO}_2$  (B) Anode for High-Voltage Aqueous Li-Ion Batteries. *Energy Storage Mater.* **2021**, *42*, 438–444.

(45) Shao, M.; Deng, J.; Zhong, F.; Cao, Y.; Ai, X.; Qian, J.; Yang, H. An All-Vanadium Aqueous Lithium Ion Battery with High Energy Density and Long Lifespan. *Energy Storage Mater.* **2019**, *18*, 92–99.